# Thickness-dependent thermal conductivity of mechanically exfoliated $\beta$ -Ga<sub>2</sub>O<sub>3</sub> thin films

Cite as: Appl. Phys. Lett. **116**, 202101 (2020); https://doi.org/10.1063/5.0004984 Submitted: 16 February 2020 • Accepted: 05 May 2020 • Published Online: 19 May 2020

Yingying Zhang, Qun Su, Jie Zhu, et al.







#### ARTICLES YOU MAY BE INTERESTED IN

A review of Ga<sub>2</sub>O<sub>3</sub> materials, processing, and devices

Applied Physics Reviews 5, 011301 (2018); https://doi.org/10.1063/1.5006941

Recent progress on the electronic structure, defect, and doping properties of Ga<sub>2</sub>O<sub>3</sub> APL Materials **8**, 020906 (2020); https://doi.org/10.1063/1.5142999

Perspective: Ga<sub>2</sub>O<sub>3</sub> for ultra-high power rectifiers and MOSFETS

Journal of Applied Physics 124, 220901 (2018); https://doi.org/10.1063/1.5062841





# Thickness-dependent thermal conductivity of mechanically exfoliated $\beta$ -Ga<sub>2</sub>O<sub>3</sub> thin films

Cite as: Appl. Phys. Lett. **116**, 202101 (2020); doi: 10.1063/5.0004984 Submitted: 16 February 2020 · Accepted: 5 May 2020 · Published Online: 19 May 2020







Yingying Zhang,¹ Qun Su,² Jie Zhu,¹,³ Sandhaya Koirala,² Steven J. Koester,² 🕞 and Xiaojia Wang¹,²,a¹ 🕞

# **AFFILIATIONS**

- Department of Mechanical Engineering, University of Minnesota, Minneapolis, Minnesota 55455, USA
- <sup>2</sup>Department of Electrical and Computer Engineering, University of Minnesota, Minneapolis, Minnesota 55455, USA
- <sup>3</sup>Key Laboratory of Ocean Energy Utilization and Energy Conservation of Ministry of Education, Dalian University of Technology, Dalian 116024, Liaoning Province, China

#### **ABSTRACT**

Beta-phase gallium oxide ( $\beta$ -Ga<sub>2</sub>O<sub>3</sub>), the most thermally stable phase of Ga<sub>2</sub>O<sub>3</sub>, has stimulated great interest in power electronics due to its ultrawide bandgap ( $\sim$ 4.9 eV) and high breakdown electric field. The relatively low thermal conductivity of  $\beta$ -Ga<sub>2</sub>O<sub>3</sub>, however, limits the device performance due to excessive temperature driven by self-heating. Recently, integrating  $\beta$ -Ga<sub>2</sub>O<sub>3</sub> thin films on substrates with high thermal conductivities has been proposed to improve heat rejection and device reliability. In this work, we prepare high-quality single-crystal  $\beta$ -Ga<sub>2</sub>O<sub>3</sub> thin films by mechanical exfoliation of bulk crystals and study their thermal transport properties. Both the anisotropic thermal conductivity of  $\beta$ -Ga<sub>2</sub>O<sub>3</sub> bulk crystals and the thickness-dependent thermal conductivity of  $\beta$ -Ga<sub>2</sub>O<sub>3</sub> thin films are measured using the time-domain thermoreflectance technique. The reduction in the thin-film thermal conductivity, compared to the bulk value, can be well explained by the size effect resulting from the enhanced phonon-boundary scattering when the film thickness decreases. This work not only provides fundamental insight into the thermal transport mechanisms for high-quality  $\beta$ -Ga<sub>2</sub>O<sub>3</sub> thin films but also facilitates the design and optimization of  $\beta$ -Ga<sub>2</sub>O<sub>3</sub>-based electronic devices.

Published under license by AIP Publishing. https://doi.org/10.1063/5.0004984

Beta-phase gallium oxide ( $\beta$ -Ga<sub>2</sub>O<sub>3</sub>), as the most thermally stable phase of Ga<sub>2</sub>O<sub>3</sub>, has been recently recognized as a promising material building block for power electronic applications,<sup>2–7</sup> attributing to its extremely large bandgap energy (~4.9 eV) and high breakdown electric field (~8 MV/cm).<sup>5,8</sup> Despite these excellent electrical properties, heat dissipation is a critical issue in limiting the performance of β-Ga<sub>2</sub>O<sub>3</sub>-based devices, <sup>5,9–14</sup> resulting from the poor thermal conductivity of  $\beta$ -Ga<sub>2</sub>O<sub>3</sub>. <sup>15–20</sup> At room temperature, the highest thermal conductivity of  $\beta$ -Ga<sub>2</sub>O<sub>3</sub> ( $\sim$ 27 W m<sup>-1</sup> K<sup>-1</sup>) is along the [010] crystalline direction. This value, however, is still one order of magnitude lower than the current state-of-the-art semiconductor materials for power electronics (typically  $\sim$ 140 W m<sup>-1</sup> K<sup>-1</sup> for silicon,  $\sim$ 350 W m<sup>-1</sup> K<sup>-1</sup> for silicon carbide, and  $\sim$ 200 W m<sup>-1</sup> K<sup>-1</sup> for gallium nitride).<sup>21</sup> To make  $\beta$ -Ga<sub>2</sub>O<sub>3</sub> competitive with other materials, more effective thermal management strategies must be explored to advance high-power and high-voltage power electronic applications based on  $\beta$ -Ga<sub>2</sub>O<sub>3</sub>. <sup>22</sup> Currently, integrating  $\beta$ -Ga<sub>2</sub>O<sub>3</sub> thin films onto substrates with high thermal conductivities (e.g., diamond) is considered a potential method to mitigate thermal issues and, thus, increase the performance and reliability of high-power  $\beta$ -Ga<sub>2</sub>O<sub>3</sub> electronic devices. <sup>13,23–28</sup> Such

an approach takes advantage of both the high thermal conductivity of the substrates and the reduction of thermal resistance (inversely proportional to the film thickness) resulting from the thin-film geometry.

To date, various growth techniques (e.g., molecular beam epitaxy, halide vapor phase epitaxy, and chemical vapor deposition) have been developed to directly synthesize  $\beta$ -Ga<sub>2</sub>O<sub>3</sub> thin films.<sup>1,5,29</sup> However, mass production of β-Ga<sub>2</sub>O<sub>3</sub> thin films using epitaxial methods on high-conductivity substrates is still challenging. Unlike the monocrystalline nature of bulk  $\beta$ -Ga<sub>2</sub>O<sub>3</sub> or homo-epitaxial  $\beta$ -Ga<sub>2</sub>O<sub>3</sub>, most of the resulting hetero-epitaxial thin films from direct growth are polycrystal-Developing high-quality  $\beta$ -Ga<sub>2</sub>O<sub>3</sub> crystals is essential for their applications in power devices since they are required to achieve the combination of high breakdown voltage and low on-state resistance to serve as the channel layers.<sup>5</sup> Recently, it has been reported that β-Ga<sub>2</sub>O<sub>3</sub> thin films can be mechanically exfoliated from bulk single crystals, eased by the mechanical properties linked to the large lattice constant along the [100] direction (12.336 Å).<sup>23,24,31,32</sup> Given the fact that large-diameter and low-defect density  $\beta$ -Ga<sub>2</sub>O<sub>3</sub> single crystals can be mass-produced using low-cost melt-grown methods, <sup>33</sup> β-Ga<sub>2</sub>O<sub>3</sub> thin films transferred from bulk crystals offer an ideal platform to study

<sup>&</sup>lt;sup>a)</sup>Author to whom correspondence should be addressed: wang4940@umn.edu

their generic material properties, taking into account the size effect and the influence of the size on performance in prototype devices.

There have been literature studies on the thermal properties of  $\beta$ -Ga<sub>2</sub>O<sub>3</sub>; however, most of those studies focused on bulk crystals and polycrystalline thin films directly grown on different substrates. <sup>15–17,30</sup> The thermal properties of single-crystal  $\beta$ -Ga<sub>2</sub>O<sub>3</sub> thin films prepared from mechanical exfoliation remain an open issue due to limited available experimental data. <sup>28</sup> In this work, we prepare high-quality single-crystal  $\beta$ -Ga<sub>2</sub>O<sub>3</sub> thin films exfoliated from bulk crystals to explore their thermal transport properties. We apply the ultrafast-laser based time-domain thermoreflectance (TDTR) technique <sup>34–36</sup> to measure the thermal conductivities of bulk and thin-film  $\beta$ -Ga<sub>2</sub>O<sub>3</sub> single crystals. The measurement data are interpreted by a kinetic-theory based model, which well elucidates the fundamental relationship between the thermal transport properties and structural features of  $\beta$ -Ga<sub>2</sub>O<sub>3</sub> thin films.

The bulk  $\beta$ -Ga<sub>2</sub>O<sub>3</sub> single-crystal wafers used in this study were purchased from a commercial vendor (Tamura Corp.). The crystal orientations of bulk samples are illustrated in Fig. 1(a): the through-plane direction is along the surface normal to the (201) crystal plane (highlighted in green), namely, the  $\pm(\overline{2}01)$  orientation. The two orthogonal in-plane directions are along the [010] and [102] orientations, respectively. As depicted in Fig. 1(a), the highly anisotropic monoclinic crystal structure of  $\beta$ -Ga<sub>2</sub>O<sub>3</sub> leads to different lattice constants along individual orientations. The much larger lattice constant along the [100] orientation implies a relatively weak bonding force, thereby enabling the cleavage of β-Ga<sub>2</sub>O<sub>3</sub> thin films from a bulk crystal via mechanical exfoliation [Fig. 1(b)].31 The exfoliation starts from peeling off an adhesive tape adhered to a bulk  $\beta$ -Ga<sub>2</sub>O<sub>3</sub> crystal along the [010] direction, leaving thick films on the tape. The tape carrying β-Ga<sub>2</sub>O<sub>3</sub> crystals is first stuck to the substrate and then gently pressed using a Q-tip to ensure adhesion. Next, the tape is quickly peeled off, which cleaves the crystals and leaves thinner flakes on the substrate. The substrate is then soaked in acetone to remove tape adhesive residues. In this study, the exfoliated films with varying thicknesses are transferred to two types of dielectric substrates: amorphous silicon dioxide (for surface-morphology characterization) and quartz (for crystalline-orientation characterization and thermal measurements). The surface morphology, structural features, and crystalline orientations of these thin-film samples are characterized using atomic force microscopy (AFM) and polarized Raman spectroscopy.

The monoclinic crystal structure also naturally leads to the anisotropic thermal conductivity of  $\beta\text{-}Ga_2O_3$  single crystals. To map the

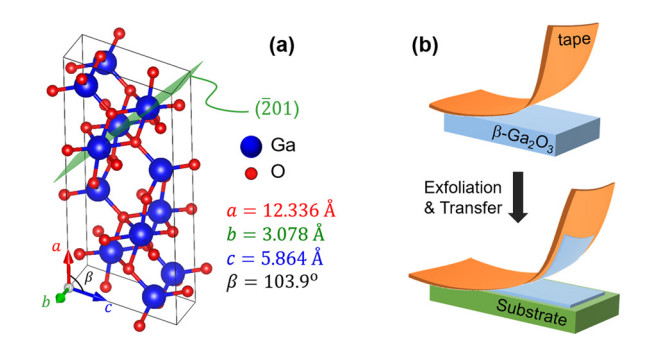


**FIG. 1.** (a) Schematic of the lattice structure of  $\beta$ -Ga<sub>2</sub>O<sub>3</sub>. (b) Mechanical exfoliation from bulk wafers to produce  $\beta$ -Ga<sub>2</sub>O<sub>3</sub> thin films.

thermal conductivities along different crystallographic directions, we conduct both standard TDTR and beam-offset measurements.<sup>37</sup> Figure 2(a) displays the typical sample stack for TDTR measurements, in which the sample is coated with a thin layer of aluminum (Al) to serve as both the heating source (by absorbing light) and the transducer (enabling monitoring of temperature).<sup>37</sup> TDTR utilizes a pump-probe configuration, where the pump beam heats the transducer layer, and the probe beam captures the temperature excursion of the sample after pump excitation. In TDTR, heat propagation into the sample from the absorbing transducer layer is treated as thermal waves at a modulation frequency f. The thermal penetration depth of thermal waves ( $\delta$ ) can be varied by controlling the modulation frequency through  $\delta = \sqrt{\Lambda/\pi Cf}$ , with C and  $\Lambda$  being the heat capacity and thermal conductivity of the sample, respectively. For thin-film samples, thermal measurements are conducted at multiple modulation frequencies. As illustrated in Fig. 2(b), a high modulation frequency produces a  $\delta$  smaller than the film thickness (d). In this case, the  $\beta$ -Ga<sub>2</sub>O<sub>3</sub> thin film is essentially thermally opaque and TDTR measurements are only sensitive to the thin-film thermal conductivity and the interfacial thermal conductance  $(G_1)$  between the Al transducer and the  $\beta$ -Ga<sub>2</sub>O<sub>3</sub> thin film. Contrarily, a low modulation frequency makes  $\delta$  larger than d [Fig. 2(c)], where the film becomes thermally thin and TDTR measurements also probe the substrate and the thermal interface between the film and the substrate  $(G_2)$ .

The surface morphology of the exfoliated thin films obtained from AFM is shown in Figs. 3(a) and 3(b) for a representative  $\beta$ -Ga<sub>2</sub>O<sub>3</sub> thin film transferred to the SiO<sub>2</sub> substrate. Figure 3(a) presents an AFM image with a larger scan area, which provides the height-uniformity information for the thin-film samples. The corresponding height histogram obtained from a line-cut of Fig. 3(a) is shown in Fig. 3(b). The left (right) peak is the height distribution of the substrate ( $\beta$ -Ga<sub>2</sub>O<sub>3</sub> thin film). The narrow distribution of the peak for  $\beta$ -Ga<sub>2</sub>O<sub>3</sub> suggests the uniformity of the film thickness over the measured area. A higher magnification AFM scan suggests the excellent surface quality of exfoliated thin films with an RMS surface roughness less than 1 nm [Fig. 3(c)]. For all thin-film samples measured using TDTR, profilometry is used to determine the film thicknesses [Fig. 3(d)]. The crystal orientations of  $\beta$ -Ga<sub>2</sub>O<sub>3</sub> thin films are measured using polarized Raman spectroscopy,<sup>38</sup> with all characteristic modes shown in Fig. 3(e). From the plot, a strong  $A_g^{(10)}$  mode can be observed, whereas the  $A_g^{(9)}$  and  $A_g^{(3)}$  modes are weaker with a

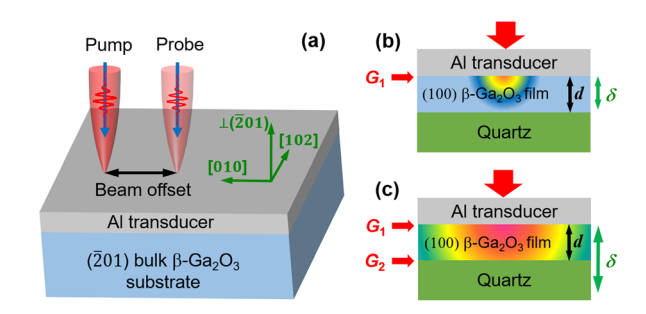


**FIG. 2.** (a) The sample stack for TDTR measurements using the beam-offset method to map the anisotropic thermal conductivity of β-Ga<sub>2</sub>O<sub>3</sub> single crystals. Schematics showing the comparison between the thermal penetration depth and the film thickness for thermal measurements at high (b) and low (c) modulation frequencies.  $G_1$  and  $G_2$  denote the interfacial thermal conductance of the Al/β-Ga<sub>2</sub>O<sub>3</sub> interface and the β-Ga<sub>2</sub>O<sub>3</sub>/substrate interface, respectively.

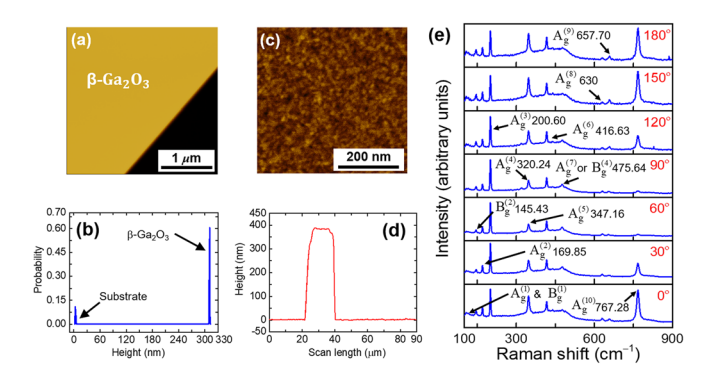


**FIG. 3.** AFM image of a representative  $\beta\text{-}\text{Ga}_2\text{O}_3$  thin film with a larger area scan (a) and the corresponding height histogram (b). (c) A higher magnification AFM image of surface morphology characterization. The height variation from dark to bright in Fig. 3(c) is 2.5 nm. (d) The height profile from representative profilometry measurements for the determination of the 384-nm film thickness. (e) Polarized Raman spectroscopy of mechanically exfoliated  $\beta\text{-}\text{Ga}_2\text{O}_3$  thin films.

negligible angular dependence. The angular modulation in the  $A_g^{(10)}$  intensity is exactly 90° off from that of  $A_g^{(4)}$ . These trends agree with the Raman signature of (100)  $\beta$ -Ga<sub>2</sub>O<sub>3</sub> and confirm the cleavage preference of the  $\beta$ -Ga<sub>2</sub>O<sub>3</sub> crystal.

For data analysis of TDTR measurements, the thickness  $(d_{Al})$ , volumetric heat capacity  $(C_{Al})$ , and thermal conductivity  $(\Lambda_{Al})$  of the Al transducer are needed as input parameters to extract the throughplane thermal conductivity of bulk  $\beta$ -Ga<sub>2</sub>O<sub>3</sub> from standard TDTR measurements.  $^{36,37,39}_{Al}$   $d_{Al}$  is determined from picosecond acoustics [Fig. 4(a)].  $^{40,41}$  Since the acoustic impedance of Al is smaller than that of  $\beta$ -Ga<sub>2</sub>O<sub>3</sub>, the curve of the first echo should be upward due to zero phase shift of the thermally induced acoustic waves. However, an

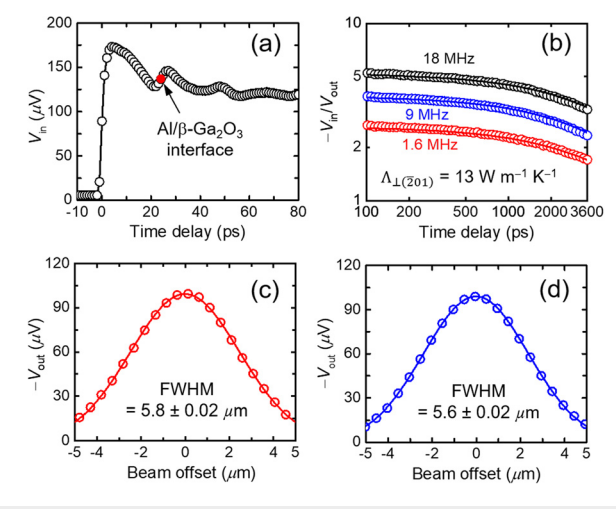


**FIG. 4.** (a) Picosecond acoustics measurements. The red dot denotes the inflection point of the acoustic echo reflected from the interface between the Al transducer and the  $\beta\text{-}\text{Ga}_2\text{O}_3$  thin film. (b) TDTR ratio signals of a bulk  $\beta\text{-}\text{Ga}_2\text{O}_3$  single crystal measured at three modulation frequencies. The solid lines are the best fits of the through-plane thermal measurement data based on the heat diffusion model. Beam-offset measurements for determining the in-plane thermal conductivity along the [010] (c) and [102] (d) crystal orientations.

asymmetric downward shape of the echo is observed in Fig. 4(a), which most likely results from a soft thin contamination layer at the interface between Al and  $\beta$ -Ga<sub>2</sub>O<sub>3</sub>. Therefore, the inflection point (red dot) between the peak and the valley (at t=24 ps) is chosen as the arrival time of the first acoustic echo returning back to the top surface, which gives a thickness of 77 nm for the Al transducer. CAl is taken from the literature to be 2.42 J cm<sup>-3</sup> K<sup>-1.42</sup> The thermal conductivity of the Al transducer is 110 W m<sup>-1</sup> K<sup>-1</sup>, converted from the electrical conductivity measured using the four-point probe method and the Wiedemann–Franz Law. Figure 4(b) depicts the representative TDTR ratio signals (- $V_{\rm in}/V_{\rm out}$ ) of a bulk  $\beta$ -Ga<sub>2</sub>O<sub>3</sub> sample measured at three modulation frequencies (1.6, 9, and 18 MHz). The solid lines in Fig. 4(b) are the best fit of TDTR data, based on a heat diffusion model for a multi-layer structure. A3,44 The fitted through–plane thermal conductivity of  $\beta$ -Ga<sub>2</sub>O<sub>3</sub> is 13 ± 1 W m<sup>-1</sup> K<sup>-1</sup> along the  $\perp$ ( $\overline{2}$ 01) direction.

The in-plane thermal conductivities of  $\beta\text{-}\text{Ga}_2\text{O}_3$  bulk crystals are measured using the beam-offset TDTR with a 20× objective lens (beam spot radius of  $w_0\approx 3~\mu\text{m})$  and at 1.6 MHz modulation.  $^{34,44,45}$  Figures 4(c) and 4(d) plot the out-of-phase signals ( $V_{\text{out}}$ ) obtained from the beam-offset measurements along the [010] and [102] crystal orientations for a bulk  $\beta\text{-}\text{Ga}_2\text{O}_3$  single crystal. The full width at half maximum (FWHM) of measured  $V_{\text{out}}$  is compared with that predicted from the heat diffusion model to obtain the in-plane thermal conductivities of  $\beta\text{-}\text{Ga}_2\text{O}_3$ . The measured thermal conductivities of two bulk  $\beta\text{-}\text{Ga}_2\text{O}_3$  single crystals (samples 1 and 2) with varying doping concentrations are summarized in Table I along different crystal orientations

Since thermal transport in  $\beta\text{-}Ga_2O_3$  is mainly carried by phonons, the phonon group velocities (or speed of sound) along different directions of propagation can significantly affect its anisotropic thermal conductivity.  $^{15,16}$  It has been reported that phonon group velocity is the largest along [010],  $^{16}$  resulting in the largest thermal conductivity along this orientation. The measurement data of our  $\beta\text{-}Ga_2O_3$  single crystals agree well with literature values (see the details in Sec. S1 of the supplementary material). We also notice that the thermal conductivity of bulk  $\beta\text{-}Ga_2O_3$  shows no apparent dependence on Sn doping, which can be attributed to the relatively small Sn doping concentrations of the measured samples. For samples with thermal transport dominated by lattice vibrations, the electronic contribution is negligible when the carrier concentration is lower than  $10^{19}$  cm  $^{-3}.^{16,20}$ 

For  $\beta$ -Ga<sub>2</sub>O<sub>3</sub> thin films, we use high-modulation frequencies of pump heating (9 and 18 MHz) to separate the intrinsic thermal conductivity of the thin films from the interfacial thermal conductance ( $G_1$ ) of the Al/ $\beta$ -Ga<sub>2</sub>O<sub>3</sub> thin film interface. The resulting thermal penetration depths at these high-modulation frequencies are less than the thin-film thickness (see the details in Sec. S2 of the supplementary material). Thus, thermal measurements at high modulation frequencies

**TABLE I.** 3D anisotropic thermal conductivities of bulk  $\beta$ -Ga<sub>2</sub>O<sub>3</sub> single crystals.

Bulk β-Ga <sub>2</sub> O <sub>3</sub>	Sn Concentration (cm <sup>-3</sup> )		$\Lambda [010] (W m^{-1} K^{-1})$	
1	$2 \times 10^{18}$	14 ± 1	$26 \pm 3$	15 ± 2
	$5 \times 10^{18}$	13 + 1	$27 \pm 3$	16 ± 2

are not sensitive to the interfacial thermal conductance  $(G_2)$  between the  $\beta$ -Ga<sub>2</sub>O<sub>3</sub> thin film and the substrate or to the substrate itself. An optical microscopic image of a representative  $\beta$ -Ga<sub>2</sub>O<sub>3</sub> thin film is shown in Fig. 5(a), and its corresponding charge-coupled-device (CCD) image during TDTR measurements is depicted in Fig. 5(b). For  $\beta$ -Ga<sub>2</sub>O<sub>3</sub> thin films with a limited width ( $\sim$ 6-7  $\mu$ m), a 50× objective lens is used to produce a much smaller beam spot size ( $\sim$ 1.3  $\mu$ m).

The through-plane thermal conductivity ( $\Lambda$ ) along the [100] direction of exfoliated  $\beta$ -Ga<sub>2</sub>O<sub>3</sub> thin films is plotted in Fig. 5(c) as a function of the film thickness (d), which exhibits an increasing trend from 4.7 to 11.5 W m<sup>-1</sup> K<sup>-1</sup> when d changes from 206 to 768 nm, approaching the bulk value of 13 W m<sup>-1</sup> K<sup>-1</sup>. The total uncertainty of the measured thin-film thermal conductivity can be calculated based on the sensitivity analysis as detailed previously.<sup>34,37</sup> Among individual parameters, the beam spot size and the transducer thickness make dominant contributions to the total uncertainty of thin-film thermal conductivity. The thickness of the thin-film sample also contributes to the uncertainty of thin-film thermal conductivity when the film is thin, but its contribution becomes negligible for thicker films. The resulting uncertainty of the through-plane thin-film thermal conductivity ranges from ~15% to 30% (see the details in Sec. S3 of the supplementary material).

To gain some physical insight into the thickness-dependent thermal conductivity of these thin films, we apply a kinetic theory-based model to better interpret the thin-film TDTR data,  $^{30}$ 

$$\Lambda = \frac{1}{3} \sum\nolimits_{j=1}^{3} \int_{0}^{\omega_{\max,j}} \hbar \omega D_{j}(\omega) \frac{\partial f_{\rm BE}}{\partial T} v_{j}^{2}(\omega) \left(\frac{1}{\tau_{\rm I}} + \frac{1}{\tau_{\rm U}} + \frac{v_{j}(\omega)}{d}\right)^{-1} d\omega,$$

$$(1)$$

where D is the phonon density of states (DOS),  $\partial f_{\rm BE}/\partial T$  is the temperature derivative of the Bose–Einstein distribution function, and the subscript "j" denotes the branch in the phonon dispersion spectrum.  $1/\tau_{\rm I}$  is the phonon-impurity scattering rate and  $1/\tau_{\rm U}$  is the Umklapp scattering rate, which are expressed as  $^{15,46}$ 

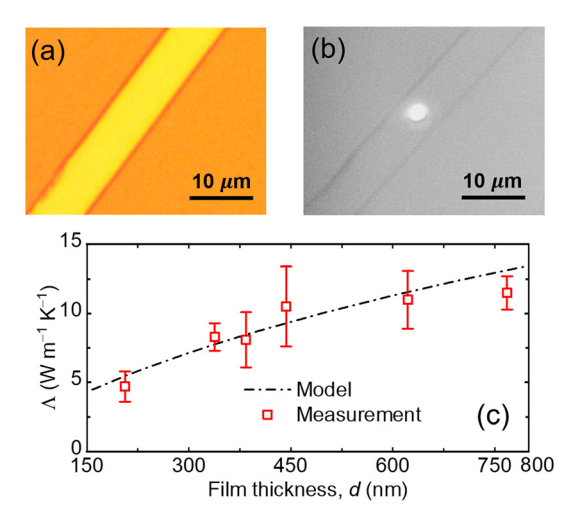


**FIG. 5.** (a) Optical microscopic image of a representative  $\beta\text{-}\text{Ga}_2\text{O}_3$  thin film. (b) The CCD image of the same  $\beta\text{-}\text{Ga}_2\text{O}_3$  thin film with the probe beam focused by a  $50\times$  objective lens. (c) Thickness-dependent thermal conductivity of  $\beta\text{-}\text{Ga}_2\text{O}_3$  thin films from both TDTR measurements (symbols) and kinetic theory-based model prediction (dashed line).

$$\left[\tau_{\rm I}^{j}(x)\right]^{-1} = \frac{V k_{\rm B}^{4} \Gamma}{4\pi \hbar^{4} v_{i}^{3}} x^{4} T^{4},\tag{2}$$

$$\left[\tau_{\rm U}^{j}(x)\right]^{-1} = \frac{k_{\rm B}^{2}\gamma_{j}^{2}}{M\hbar v_{i}^{2}\theta_{j}}x^{2}T^{3}e^{-\frac{\theta_{j}}{3T}},\tag{3}$$

where  $V=1.0587\times 10^{-29}$  m³/atom and  $M=6.2231\times 10^{-26}$  kg/atom for  $\beta$ -Ga<sub>2</sub>O<sub>3</sub><sup>15</sup> and  $x=\hbar\omega/k_{\rm B}T$ . Literature values are used for the Grüneisen parameters  $\gamma_j$  ( $\gamma_{\rm L}=1.3$  and  $\gamma_{\rm T}=0.95$ ), Debye temperature of different phonon branches  $\theta_j$  ( $\theta_{\rm L}=190$  K,  $\theta_{\rm T1}=125$  K, and  $\theta_{\rm T2}=105$  K,), the cutoff frequencies of different branches  $\omega_{\rm max,j}(\omega_{\rm max,L}=4.0$  THz,  $\omega_{\rm max,T1}=2.6$  THz,  $\omega_{\rm max,T2}=2.2$  THz), and the mass-fluctuation phonon-scattering parameter  $\Gamma$  ( $\Gamma=2.2399\times 10^{-4}$ ). In this calculation, the contribution from optical phonons is neglected, considering the relatively small impact of optical phonons on the thermal conductivity of  $\beta$ -Ga<sub>2</sub>O<sub>3</sub> bulk crystals along the [100] direction reported in the literature. To take into account the zone boundary effect, a sine-shape dispersion of the DOS is applied for the three acoustic branches, with  $\alpha$  being the lattice constant,  $\alpha$ 

$$D_{j}(\omega) = \frac{4\left[\sin^{-1}\left(\omega/\omega_{\max,j}\right)\right]^{2}}{\pi\omega_{\max,j}a^{3}\sqrt{1-\left(\omega/\omega_{\max,j}\right)^{2}}},\tag{4}$$

$$v_j(\omega) = \frac{\omega_{\max,j}a}{2}\sqrt{1 - \left(\omega/\omega_{\max,j}\right)^2}.$$
 (5)

As seen from Fig. 5(c), a reasonable agreement is achieved between the measured thermal conductivity and the model predicted values based on Eq. (1). Since the phonon-boundary scattering rate is dominant over the Umklapp and impurity scattering rates, it suggests that the thickness dependence of the through-plane thermal conductivity of single-crystal  $\beta$ -Ga<sub>2</sub>O<sub>3</sub> thin films can mainly be attributed to the phonon-boundary scattering described in the literature (the details are provided in Sec. S4 of the supplementary material).  $^{30,46,48}$ 

Besides thermal conductivity, the values of interfacial thermal conductance can also be obtained from TDTR measurements. The values of G1 derived from TDTR experiments range from 30 to 150 MW m<sup>-2</sup> K<sup>-1</sup> for the Al/ $\beta$ -Ga<sub>2</sub>O<sub>3</sub> interface, depending on the different surface treatment conditions (see the details in Sec. S5 of the supplementary material). The values of  $G_2$  are measured to be  $15 \pm 4.5 \,\mathrm{MW} \;\mathrm{m}^{-2} \,\mathrm{K}^{-1}$  for one thin-film sample (338 nm) at 1.6 MHz, comparable to literature values of the van der Waals-bonded thermal interface between transferred  $\beta$ -Ga<sub>2</sub>O<sub>3</sub> thin films and diamond.<sup>28</sup> It is worth noting that when the thickness of  $\beta$ -Ga<sub>2</sub>O<sub>3</sub> thin films reduces to several nanometers and becomes comparable with the interfacial thickness, the thermal transport across the  $\beta$ -Ga<sub>2</sub>O<sub>3</sub>/substrate interface will be of great importance for the overall heat dissipation. Considering that  $G_2$  can be influenced by different substrates and interfacial properties (e.g., roughness and/or contamination layers), caution should be taken with surface cleaning and treatments prior to transferring thin films onto substrates. Further systematic investigation will be needed to reveal more details of how the substrates and the interfacial properties can impact the interfacial thermal transport.

This work experimentally studied the thermal properties of bulk and thin-film  $\beta\text{-}Ga_2O_3$  single crystals. For bulk crystals, the throughplane thermal conductivity is measured to be  $13\pm1\,\text{W}$  m $^{-1}$  K $^{-1}$  along the  $\pm(\overline{2}01)$  direction and the in-plane thermal conductivities

are  $16\pm2\,\mathrm{W}$  m<sup>-1</sup> K<sup>-1</sup> and  $27\pm3\,\mathrm{W}$  m<sup>-1</sup> K<sup>-1</sup> along the [102] and [010] directions, respectively. Sn doping has a negligible effect on the thermal conductivity due to the low carrier concentration ( $<10^{19}\,\mathrm{cm}^{-3}$ ) of the measured samples. For thin-film samples with thicknesses varying from 206 to 768 nm, the through-plane thermal conductivity along the [100] direction increases from 4.7 to  $11.5\,\mathrm{W}\,\mathrm{m}^{-1}\,\mathrm{K}^{-1}$ , approaching the bulk value ( $13\,\mathrm{W}\,\mathrm{m}^{-1}\,\mathrm{K}^{-1}$ ) at 768 nm. A kinetic theory-based model explains the experimental data by attributing the thickness dependence of thermal conductivity to the enhanced phonon-boundary scattering at reduced thicknesses. These thermal studies of both bulk and thin-film  $\beta$ -Ga<sub>2</sub>O<sub>3</sub> single crystals have the potential to enhance the design of future thermally aware  $\beta$ -Ga<sub>2</sub>O<sub>3</sub>-based power electronic devices.

See the supplementary material for the details of measurement sensitivity and uncertainty analyses, comparison with literature data, and scattering rates for model calculations.

We gratefully acknowledge funding support from the National Science Foundation through the University of Minnesota MRSEC under Award No. DMR-1420013 and from the Minnesota Futures Grant. Sample preparation was conducted in the Minnesota Nano Center, which was supported by the NSF through the National Nano Coordinated Infrastructure Network (NNCI No. ECCS-1542202).

### **DATA AVAILABILITY**

The data that support the findings of this study are available within this article or from the corresponding author upon reasonable request.

## REFERENCES

- <sup>1</sup>M. Higashiwaki, K. Sasaki, H. Murakami, Y. Kumagai, A. Koukitu, A. Kuramata, T. Masui, and S. Yamakoshi, Semicond. Sci. Technol. 31(3), 034001 (2016).
- <sup>2</sup>M. Higashiwaki, K. Konishi, K. Sasaki, K. Goto, K. Nomura, Q. Tu Thieu, R. Togashi, H. Murakami, Y. Kumagai, and B. Monemar, Appl. Phys. Lett. 108(13), 133503 (2016).
- <sup>3</sup>M. Higashiwaki, K. Sasaki, T. Kamimura, M. Hoi Wong, D. Krishnamurthy, A. Kuramata, T. Masui, and S. Yamakoshi, Appl. Phys. Lett. **103**(12), 123511 (2013).
- <sup>4</sup>M. Higashiwaki, K. Sasaki, A. Kuramata, T. Masui, and S. Yamakoshi, Appl. Phys. Lett. **100**(1), 013504 (2012).
- <sup>5</sup>H. Zhou, J. Zhang, C. Zhang, Q. Feng, S. Zhao, P. Ma, and Y. Hao, J. Semicond. **40**(1), 011803 (2019).
- <sup>6</sup>M. Hoi Wong, K. Sasaki, A. Kuramata, S. Yamakoshi, and M. Higashiwaki, IEEE Electron Device Lett. **37**(2), 212 (2016).
- J. Pearton, F. Ren, M. Tadjer, and J. Kim, J. Appl. Phys. 124(22), 220901 (2018).
   A. E. Romanov, S. I. Stepanov, V. I. Nikolaev, and V. E. Bougrov, Rev. Adv. Mater. Sci. 44, 63 (2016).
- 9S. Shin, M. A. Wahab, M. Masuduzzaman, K. Maize, J. Gu, M. Si, A. Shakouri, D. Y. Peide, and M. A. Alam, IEEE Trans. Electron Devices 62(11), 3516 (2015).
- <sup>10</sup>J. W. Pomeroy, C. Middleton, M. Singh, S. Dalcanale, M. J. Uren, M. H. Wong, K. Sasaki, A. Kuramata, S. Yamakoshi, and M. Higashiwaki, IEEE Electron Device Lett. 40(2), 189 (2019).
- <sup>11</sup>M. Hoi Wong, Y. Morikawa, K. Sasaki, A. Kuramata, S. Yamakoshi, and M. Higashiwaki, Appl. Phys. Lett. **109**(19), 193503 (2016).
- <sup>12</sup>B. Chatterjee, A. Jayawardena, E. Heller, D. W. Snyder, S. Dhar, and S. Choi, Rev. Sci. Instrum. 89(11), 114903 (2018).
- <sup>13</sup>B. Chatterjee, K. Zeng, C. D. Nordquist, U. Singisetti, and S. Choi, IEEE Trans. Compon., Packag. Manuf. Technol. 9(12), 2352 (2019).

- <sup>14</sup>N. A. Blumenschein, N. A. Moser, E. R. Heller, N. C. Miller, A. J. Green, A. Popp, A. Crespo, K. Leedy, M. Lindquist, and T. Moule, IEEE Trans. Electron Devices 67(1), 204 (2020).
- <sup>15</sup>P. Jiang, X. Qian, X. Li, and R. Yang, Appl. Phys. Lett. 113(23), 232105 (2018).
   <sup>16</sup>Z. Guo, A. Verma, X. Wu, F. Sun, A. Hickman, T. Masui, A. Kuramata, M. Higashiwaki, D. Jena, and T. Luo, Appl. Phys. Lett. 106(11), 111909 (2015).
- <sup>17</sup>M. Handwerg, R. Mitdank, Z. Galazka, and S. F. Fischer, Semicond. Sci. Technol. 30(2), 024006 (2015).
- <sup>18</sup>V. I. Nikolaev, V. Maslov, S. I. Stepanov, A. I. Pechnikov, V. Krymov, I. P. Nikitina, L. I. Guzilova, V. E. Bougrov, and A. E. Romanov, J. Cryst. Growth. 457, 132 (2017).
- <sup>19</sup>N. Blumenschein, M. Slomski, P. P. Paskov, F. Kaess, M. H. Breckenridge, J. F. Muth, and T. Paskova, in paper presented at the Oxide-Based Materials and Devices IX (2018).
- <sup>20</sup>M. Slomski, N. Blumenschein, P. P. Paskov, J. F. Muth, and T. Paskova, J. Appl. Phys. **121**(23), 235104 (2017).
- <sup>21</sup>Q. Zheng, C. Li, A. Rai, J. H. Leach, D. A. Broido, and D. G. Cahill, Phys. Rev. Mater. 3(1), 014601 (2019).
- <sup>22</sup>M. A. Mastro, A. Kuramata, J. Calkins, J. Kim, F. Ren, and S. J. Pearton, ECS J. Solid State Sci. Technol. 6(5), P356 (2017).
- 23J. Noh, M. Si, H. Zhou, M. J. Tadjer, and P. D. Ye, "The impact of substrates on the performance of top-gate p-Ga203 field-effect transistors: record high drain current of 980 mA/mm on diamond," 2018 76th Device Research Conference (DRC), Santa Barbara, CA, 24-27 June 2018 (IEEE, 2018), pp. 1-2.
- <sup>24</sup>H. Zhou, K. Maize, J. Noh, A. Shakouri, and P. D. Ye, ACS Omega 2(11), 7723 (2017).
- <sup>25</sup>J. Oh, J. Ma, and G. Yoo, Results Phys. **13**, 102151 (2019).
- <sup>26</sup>C.-H. Lin, N. Hatta, K. Konishi, S. Watanabe, A. Kuramata, K. Yagi, and M. Higashiwaki, Appl. Phys. Lett. 114(3), 032103 (2019).
- 27 Z. Cheng, V. D. Wheeler, T. Bai, J. Shi, M. J. Tadjer, T. Feygelson, K. D. Hobart, M. S. Goorsky, and S. Graham, Appl. Phys. Lett. 116(6), 062105 (2020).
- <sup>28</sup>Z. Cheng, L. Yates, J. Shi, M. J. Tadjer, K. D. Hobart, and S. Graham, APL Mater. 7(3), 031118 (2019).
- <sup>29</sup>S. Rafique, L. Han, and H. Zhao, ECS Trans. 80(7), 203 (2017).
- <sup>30</sup>C. J. Szwejkowski, N. C. Creange, K. Sun, A. Giri, B. F. Donovan, C. Constantin, and P. E. Hopkins, J. Appl. Phys. 117(8), 084308 (2015).
- <sup>31</sup>W. Sik Hwang, A. Verma, H. Peelaers, V. Protasenko, S. Rouvimov, H. Xing, A. Seabaugh, W. Haensch, C. Van de Walle, and Z. Galazka, Appl. Phys. Lett. 104(20), 203111 (2014).
- <sup>32</sup>H. Zhou, M. Si, S. Alghamdi, G. Qiu, L. Yang, and D. Y. Peide, IEEE Electron Device Lett. 38(1), 103 (2017).
- <sup>33</sup>Z. Galazka, K. Irmscher, R. Uecker, R. Bertram, M. Pietsch, A. Kwasniewski, M. Naumann, T. Schulz, R. Schewski, and D. Klimm, J. Cryst. Growth. 404, 184 (2014).
- <sup>34</sup>J. Zhu, H. Park, J.-Y. Chen, X. Gu, H. Zhang, S. Karthikeyan, N. Wendel, S. A. Campbell, M. Dawber, and X. Du, Adv. Electron. Mater. 2(5), 1600040 (2016).
- <sup>35</sup>J. Zhu, Y. Zhu, X. Wu, H. Song, Y. Zhang, and X. Wang, Appl. Phys. Lett. 108(23), 231903 (2016).
- 36 D. G. Cahill, Rev. Sci. Instrum. 75(12), 5119 (2004).
- <sup>37</sup>J. Zhu, X. Wu, D. M. Lattery, W. Zheng, and X. Wang, Nanosc. Microsc. Therm. 21(3), 177 (2017).
- <sup>38</sup>C. Kranert, C. Sturm, R. Schmidt-Grund, and M. Grundmann, Sci. Rep. 6, 35964 (2016).
- A. J. Schmidt, X. Chen, and G. Chen, Rev. Sci. Instrum. 79(11), 114902 (2008).
   G. T. Hohensee, W.-P. Hsieh, M. D. Losego, and D. G. Cahill, Rev. Sci. Instrum. 83(11), 114902 (2012).
- <sup>41</sup>G. L. Eesley, B. M. Clemens, and C. A. Paddock, Appl. Phys. Lett. **50**(12), 717 (1987).
- <sup>42</sup>D. A. Ditmars, C. A. Plint, and R. C. Shukla, Int. J. Thermophys. **6**(5), 499 (1985).
- <sup>43</sup>J. Zhu, D. Tang, W. Wang, J. Liu, K. W. Holub, and R. Yang, J. Appl. Phys. 108(9), 094315 (2010).
- 44 Z. Ge, D. G. Cahill, and P. V. Braun, J. Phys. Chem. B 108, 18870 (2004).
- 45 J. P. Feser and D. G. Cahill, Rev. Sci. Instrum. 83(10), 104901 (2012).
- 46D. T. Morelli, J. P. Heremans, and G. A. Slack, Phys. Rev. B 66(19), 195304 (2002).
- <sup>47</sup>M. D. Santia, N. Tandon, and J. D. Albrecht, Appl. Phys. Lett. **107**(4), 041907 (2015).
- <sup>48</sup>J. R. Lukes, D. Y. Li, X.-G. Liang, and C.-L. Tien, J. Heat Transfer 122(3), 536 (2000).